

# Lattice Vibrations of Natural Seraphinite Gemstone Probed by Terahertz Time-Domain Spectroscopy

Daehoon Han, Heejae Jeong, Yunheung Song, Jai Seok Ahn, and Jaewook Ahn

**Abstract**—In this paper, we report the first observation of terahertz (THz) frequency lattice vibrations in naturally occurring seraphinite gemstones. Seraphinite is a particular form of clinocllore minerals in the chlorite group, and the THz frequency response of any chlorite minerals has been unknown. Here, we show, based on our THz time-domain spectroscopic measurements, that there are three absorption modes at 0.8, 0.96, and 1.2 THz, respectively. The 0.96 THz mode is, in particular, strong and narrow ( $Q = 8$ ), comparable to the previously reported 0.53 THz mode in  $\alpha$ -lactose monohydrate. Also, a polarization-dependent study reveals the  $A_u(z')$ -symmetry of the 0.8 and 1.2 THz modes and the  $B_u(x', y')$ -symmetry of the 0.96 THz mode. The anisotropy of the phonon-polariton dispersions shows an excellent agreement with theoretical analysis based on Kurosawa formula.

**Index Terms**—Lattice vibration, seraphinite, spectroscopy, terahertz absorption.

## I. INTRODUCTION

THE science and technology involved with terahertz (THz) frequency electromagnetic waves [1] have tremendously progressed during the past decades, providing an intellectual and technological bridge between traditional studies in optics and microwave electronics [2]. In particular, THz time-domain spectroscopy (THz-TDS) [3] has been playing a crucial role in investigating new properties and phenomena of materials. Many materials have spectral fingerprints in THz frequency range, and, in that regards, the spectroscopic capability utilizing ultra-broadband THz frequency waves has foretold a rich variety of potential applications including polymorph material classification [4], hazardous material detection, functional study of bio-medical materials [5], high-speed in-door communications, high-altitude telecommunications, quality control and process monitoring, etc [1].

THz-TDS directly measures electric-field responses of materials, thus spectral phase information can be obtained without resorting to the Kramers-Kronig relationship [6]. When a THz pulse passes through a sample of thickness  $d$ , the transmission

amplitude spectrum  $\rho(\omega)$  and the transmission phase spectrum  $\phi(\omega)$  can be obtained by

$$\tilde{T}(\omega) = \frac{\tilde{E}_s(\omega)}{\tilde{E}_r(\omega)} = \rho(\omega)e^{i\phi(\omega)}\tilde{F}(\omega) \quad (1)$$

where  $\tilde{E}_s(\omega)$  and  $\tilde{E}_r(\omega)$  are the transmitted electric-fields with and without the sample, respectively, and  $\tilde{F}(\omega)$  is the Fabry-Pérot effect caused by internal reflections in the sample. The complex refractive index of sample, defined by  $\tilde{n} = n + i\kappa$ , is then obtained, for example, by the fixed point iteration method [7], as follows:

$$n(\omega) = n_a + \frac{c}{\omega d}\phi(\omega), \quad \kappa(\omega) = -\frac{c}{\omega d}\log \rho(\omega) \quad (2)$$

where  $n_a$  is the refractive index of air and  $c$  is the speed of light. The extinction coefficient is also obtained by

$$\alpha(\omega) = \frac{2\omega}{c}\kappa(\omega). \quad (3)$$

Dielectric properties have been studied in various materials, including crystal dielectrics, semiconductors [3], plastics [8], explosives [9], liquids [10], biomaterials [11], metamaterials [12], silicate glasses [13] and natural mineral compounds [14], [15], etc. Furthermore, advanced optical properties such as birefringence [16], anisotropic single crystal measurement [17]–[19], optical activity [20], magneto/electro-optical effects [21], and electromagnons [22] in the THz frequency range are also under active investigation.

In this paper, we report the first observation of strong absorption modes of naturally occurring seraphinite in THz frequency range. Seraphinite is the special name for a particular form of a clinocllore mineral of gem-grade quality, which exhibits a green feather-like uneven color distribution of chatoyant fibers, based on which appearance the Greek word “seraphim” meaning the wings of a celestial being is used. Clinocllore, often referred to as chlorite jade although it is not a real jade [23], is a member of the chlorite group [24]. Seraphinite contains Mg with the chemical formula [25] of  $(\text{Mg}, \text{Fe}^{2+})_5\text{Al}(\text{Si}_3\text{Al})\text{O}_{10}(\text{OH})_8$ . Fig. 1 shows the atomic structure of seraphinite [26], a monoclinic layered structure in the space group C2/m at room temperature [27]. The substructure of seraphinite consists of two different layers, a talc-like layer and a brucite-like layer [28], as shown in Fig. 1. The both layers have mainly octahedra with magnesium (or aluminum) atoms centered around oxygen atoms, while the talc-like layer has additional  $\text{SiO}_4$  tetrahedras at the top and the bottom of each octahedra. Since the layers are electrically charged (the talc-like layer is negative and the brucite-like layer is positive), the pseudo random piling in clinocllore could induce polariton

Manuscript received March 13, 2015; revised June 14, 2015; accepted July 30, 2015. Date of publication September 24, 2015; date of current version November 23, 2015. This work was supported by National Research Foundation of Korea under the Basic Science Research Program 2013R1A2A2A05005187. (Corresponding author: Jaewook Ahn.)

D. Han, H. Jeong, Y. Song, and J. Ahn are with the Department of Physics, KAIST, Daejeon 305-701, Korea.

J. S. Ahn is with the Department of Physics, Pusan National University, Pusan 609-735, Korea.

Color versions of one or more of the figures in this paper are available online at <http://ieeexplore.ieee.org>.

Digital Object Identifier 10.1109/TTHZ.2015.2464087

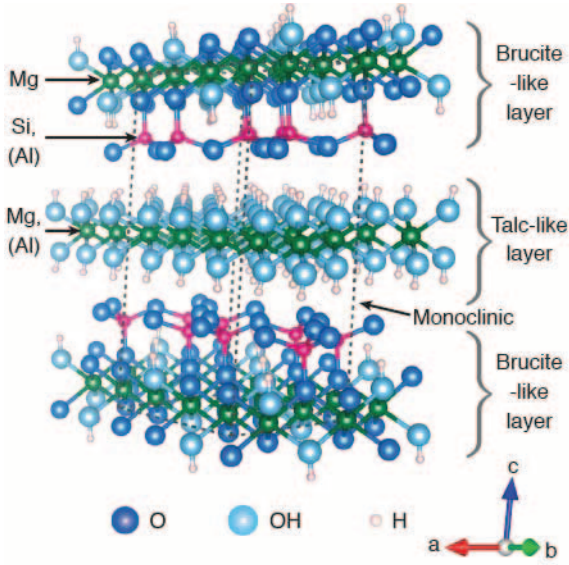


Fig. 1. Atomic structure of seraphinite with atomic position parameters from [26]. The unit cell parameters are  $a = 5.350(3)$ ,  $b = 9.267(5)$ ,  $c = 14.27(1)$ , and  $\gamma(\angle(a, c)) = 96.35(5)^\circ$ .

behaviors upon light illumination. We show that the absorptions at 0.8, 1.2, and 0.96 THz frequencies (26.64, 39.96, and 31.97  $\text{cm}^{-1}$  in wave numbers, respectively) reported in this paper are the phonon-polariton coupled modes [29] for infrared (IR)-active optic phonons with  $A_u(z')$  and  $B_u(x', y')$ -symmetries [30]–[32].

## II. EXPERIMENTAL PROCEDURE

All experiments were performed with a conventional THz-TDS setup used in earlier reports [14]. Briefly, ultrafast laser pulses, wavelength-centered at 840 nm, were produced from a Ti:sapphire mode-locked laser oscillator operating at a repetition rate of 80 MHz and used to generate THz pulses from a photo-conductive antenna (PCA). Upon illumination of each laser pulse of a 120-fs-short pulse duration, a THz pulse of less than a picosecond pulse duration was produced. The electric-field of the THz pulse was measured with an electro-optic sampling by another optical pulse (the probe pulse) split off from the first laser pulse. The polarization of the optical probe pulse through a (110)-oriented ZnTe crystal with a thickness of 1 mm was rotated with an angle linearly proportional to the electric-field amplitude of the co-propagating THz pulse via the Pockels effect. The whole setup was covered by an acrylic box purged with dry air to eliminate water vapor absorptions.

Samples were prepared with two different cuts, parallel ( $\parallel$ -cut and perpendicular ( $\perp$ )-cut, with respect to the feather-like pattern. The sample thickness was  $d = 0.96$  mm for  $\perp$ -cut and 0.8 mm for  $\parallel$ -cut, and the sample area was over  $5 \times 5$   $\text{mm}^2$ . The sample rotation was performed by a motorized rotation mount and the sample was attached on the aluminum metal holder with a hole diameter of 5 mm, which is sufficiently large compared with the Rayleigh diffraction limit corresponding to the measured THz frequency range.

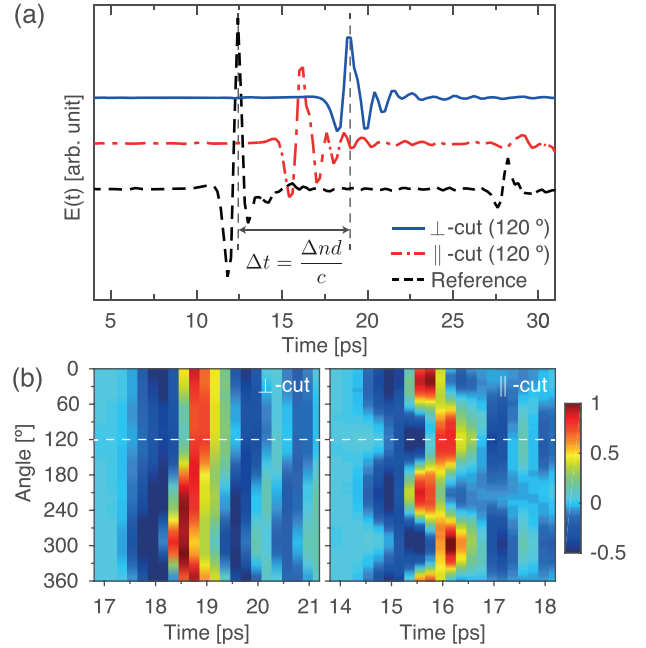


Fig. 2. (a) Measured electric-field amplitudes of a THz pulse at the azimuthal angle of  $120^\circ$  transmitted through the  $\perp$ -cut (blue solid line) and  $\parallel$ -cut (red dash-dot line) seraphinite sample, respectively, compared with the reference signal (black dotted line). The time delay  $\Delta t$  between the main peaks of the two signals corresponds to the differential index  $\Delta n$  between the sample ( $n_g = 3.0$ ) and air ( $n_a = 1$ ) times the thickness ( $d = 0.96$  mm) divided by  $c$ . (b) Polarization-dependent THz waveforms measured by varying the azimuthal angle of the  $\perp$ -cut and  $\parallel$ -cut seraphinites with respect to linearly-polarized incident THz waves. It is noted that the THz waveforms are normalized for the sake of comparison.

## III. RESULTS

When the THz-TDS recorded the time-domain electric-field amplitude of THz pulses transmitted through the sample, the typical measurements are as shown in Fig. 2(a). For the transmitted THz pulses through the  $\perp$ -cut and  $\parallel$ -cut samples, respectively, the THz pulses (blue solid and red dash-dot lines, respectively) are time-delayed from the reference peak (black dotted line) and the time delay is given by  $\Delta t = (n_g - n_a)d/c$ , where  $n_g$  was the group index of sample. By varying the azimuthal angle of the samples, measurements were repeated to plot the measured THz waveforms as shown in Fig. 2(b). The periodical delay of the peak position in time results from the birefringence of the seraphinite.

When the time-domain data is converted to the frequency-domain through Fourier transformation, the index of refraction  $n(\omega)$  and the extinction coefficient  $\alpha(\omega)$  are obtained respectively by comparing the spectral responses with and without the sample. Both the real and imaginary parts of the electric susceptibility, or the index of refraction and the absorption, of the sample are obtained from (2) and (3), through the fixed point iteration method [7]. Fig. 3 shows the experimental result. The index of refraction  $n(\omega, \theta)$  and the extinction coefficient  $\alpha(\omega, \theta)$  of the  $\perp$ -cut and  $\parallel$ -cut seraphinites are shown in Fig. 3(a)–(d), as a function of the azimuthal angle ( $\theta$ ) with respect to the THz polarization direction.

### A. The Strong Absorption Mode at 0.96 THz

When the extinction coefficient at  $\theta = 120^\circ$  in Fig. 3(b) of the  $\perp$ -cut seraphinite is fitted with two Lorentzian line-shapes [33],

TABLE I  
THE CHARACTERISTICS OF THE STRONG ABSORPTION LINE OF  $\perp$ -CUT SERAPHINITE AT 0.96 THz

Materials	Fitting function	$\nu$ [THz]	$\Delta\nu$ [THz]	$Q$ -factor ( $\nu/\Delta\nu$ )	Oscillator strength $f$	Technique	References
Seraphinite	Lorentzian	0.960	0.120	8.14	0.072	THz-TDS	This work
$\alpha$ -Lactose monohydrate	Lorentzian	0.525	0.069	7.60	0.016	THz-TDS	Ref. [34]

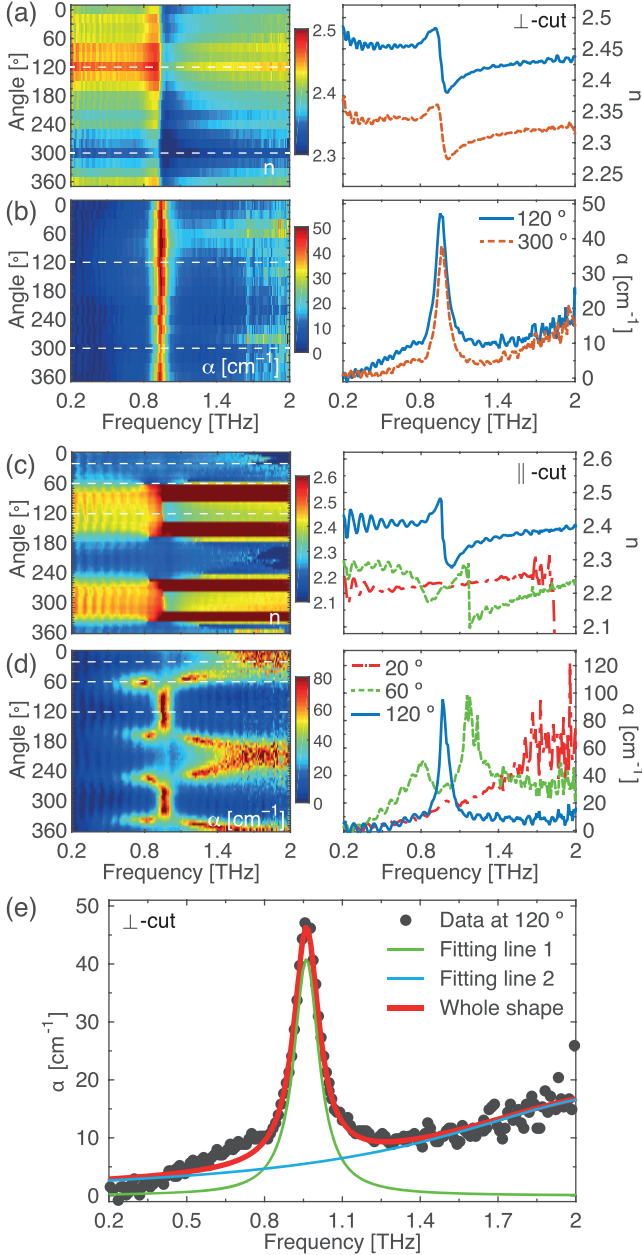


Fig. 3. (a), (c) The index of refraction  $n(\omega, \theta)$  for  $\theta \in \{0, \dots, 360\}$  and (b), (d) the extinction coefficient  $\alpha(\omega, \theta)$  for  $\theta \in \{0, \dots, 360\}$  of  $\perp$ -cut and  $\parallel$ -cut seraphinites measured as a function of the azimuthal angle ( $\theta$ ) with respect to the THz polarization direction, respectively; (a)  $n_{\perp}(\omega, 120^{\circ})$  and  $n_{\perp}(\omega, 300^{\circ})$ , (b)  $\alpha_{\perp}(\omega, 120^{\circ})$  and  $\alpha_{\perp}(\omega, 300^{\circ})$ . The strong absorption mode is measured at 0.96 THz. (c), (d)  $n_{\parallel}(\omega, \theta)$  and  $\alpha_{\parallel}(\omega, \theta)$  at  $\theta = 20^{\circ}$ ,  $60^{\circ}$ , and  $120^{\circ}$ . (e) The strong absorption mode of  $\perp$ -cut seraphinite. When the extinction coefficient at azimuthal angle of  $\theta = 120^{\circ}$  of  $\perp$ -cut seraphinite was fitted to two Lorentzian functions, the 0.96 THz absorption peak has a linewidth of 0.12 THz (FWHM).

the 0.96 THz ( $\nu$ ) strong absorption exhibits a full width at half maximum (FWHM) of  $\Delta\nu = 0.12$  THz, as shown in Fig. 3(e).

The corresponding  $Q$  factor ( $\nu/\Delta\nu$ ) of 8.14 is extremely high comparable to the well-known THz absorption peak at 0.53 THz of  $\alpha$ -lactose monohydrate [34]. Since the  $Q$  factor characterizes the resonance narrowness, materials with a large  $Q$ , in particular of a solid-state material, can be useful for making devices such as band-pass filters and frequency standards, etc. The oscillator strength [35] defined by  $f = 8\pi^2\sigma_{\max}\Delta\omega/\omega^2$ , where  $\sigma = \omega \text{Im}[\tilde{\epsilon}(\omega)]/4\pi$  is conductivity, for the 0.96 THz mode at  $\theta = 120^{\circ}$  of  $\perp$ -cut seraphinite is  $f = 0.072$ . The retrieved parameters for the 0.96 THz absorption peak are summarized in Table I.

### B. The Dielectric Tensor for a Monoclinic Structure

The crystalline structure of seraphinite belongs to the space group of C2/m. The factor group analysis [36] predicts that the dipole momenta of  $A_u$  and  $B_u$  modes are respectively inclined along the  $z'$ -axis and placed on the  $ab$ -plane, where  $a$ ,  $b$ , and  $c$  denote monoclinic crystal axes and  $x'$ ,  $y'$ , and  $z'$  the principal coordinates. The principle coordinates of this crystal is related to the crystallographic coordinates ( $a, b, c$ ) as follows:  $x' \parallel a$ ,  $y' \parallel b$ , and  $\angle(a, c) = 96.35(5)^{\circ}$  [26].

To understand the polarization dependence of the extinction coefficients in Fig. 3(c) and (d), we consider the (relative) dielectric tensor  $\tilde{\epsilon}(\omega)$  represented with the principal coordinates ( $x', y', z'$ )

$$\tilde{\epsilon}(\omega) = \begin{bmatrix} \tilde{\epsilon}_{x'x'}(\omega) & \tilde{\epsilon}_{x'y'}(\omega) & 0 \\ \tilde{\epsilon}_{x'y'}(\omega) & \tilde{\epsilon}_{y'y'}(\omega) & 0 \\ 0 & 0 & \tilde{\epsilon}_{z'z'}(\omega) \end{bmatrix}. \quad (4)$$

The nonzero components of the dielectric tensor in (4) are described by a generalized Drude-Lorentz model [37], [38] as follows:

$$\tilde{\epsilon}_{ij}(\omega) = \epsilon_{ij}^{\infty} + \sum_{n \in \{A_u, B_u\}} \tilde{S}_n(\omega) \Gamma_i^n \Gamma_j^n \quad (5)$$

for  $i, j \in \{x', y', z'\}$ , where  $\epsilon_{ij}^{\infty}$  denotes the high frequency contribution and the angle dependence factors are given by

$$\Gamma_{x'}^n = \sin \theta_n \cos \phi_n, \quad \Gamma_{y'}^n = \sin \theta_n \sin \phi_n, \quad \Gamma_{z'}^n = \cos \theta_n. \quad (6)$$

The complex oscillator term  $\tilde{S}_n$  is defined by

$$\tilde{S}_n = \frac{\omega_{p,n}}{\omega_{0,n}^2 - \omega^2 - i\gamma_n\omega} \quad (7)$$

where  $\omega_{p,n}$ ,  $\omega_{0,n}$ ,  $\gamma_n$  are the plasma frequency, the transverse frequency, and the damping coefficient of the  $n$ th mode that belong to the  $A_u$  modes and  $B_u$  modes, respectively. It is noted that  $\theta_n$  and  $\phi_n$  denote the polar angle and the azimuthal angle between the  $n$ th dipole moment and the  $z'$ -axis as shown in Fig. 4(a).

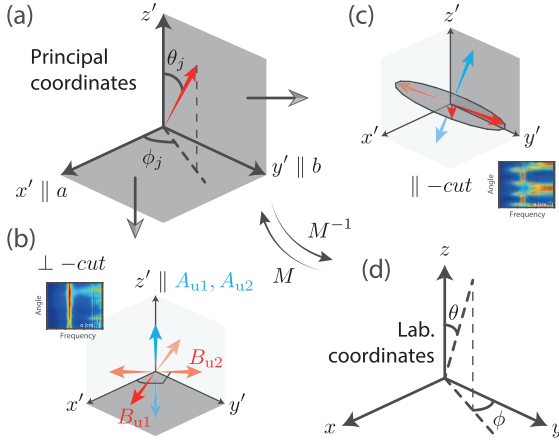


Fig. 4. (a) Principle coordinates. (b) Sample coordinates of the  $\perp$ -cut sample. (c) Sample coordinates of the  $\parallel$ -cut sample. (d) Lab-frame coordinates are transformed from the principle or sample coordinates via  $M$ , where  $\theta_j$  and  $\phi_j$  represent the polar angle and the azimuthal angle between the  $j$ th dipole moment (red arrow) and the  $z'$ -axis. The crystal surface is represented by dark gray color in each figure.

### C. Relation Between the Polarizability and the Susceptibility

From the electromagnetic theory [39], the polarizability  $P$  and the complex refractive index  $n$  of a material are given in terms of the effective susceptibility  $\chi_{\text{eff}}$  [33] by

$$\tilde{P}(\omega, \theta) = \epsilon_0 \tilde{\chi}_{\text{eff}}(\omega, \theta) \tilde{E} \quad (8)$$

$$\tilde{n}(\omega, \theta) = \sqrt{1 + \tilde{\chi}_{\text{eff}}(\omega, \theta)} \quad (9)$$

where  $\theta$  is the polarization angle. According to the complex refractive index defined by  $\tilde{n} = n + i\kappa$ , the effective susceptibility in (9) can be obtained throughout the measured THz frequency range as

$$\tilde{\chi}_{\text{eff}}(\omega, \theta) = [n(\omega, \theta) + i\kappa(\omega, \theta)]^2 - 1. \quad (10)$$

Therefore, the angle dependence of the polarizability  $\tilde{P}$  is the same as that of the susceptibility  $\tilde{\chi}_{\text{eff}}$  obtained from the complex refractive index  $\tilde{n}$  [39].

### D. Isotropic Excitation Behavior in the $\perp$ -Cut Seraphinite

In a monoclinic crystal, the dipole moments of  $A_u(z')$  modes are aligned with the  $z'$ -axis and  $B_u(x', y')$  modes are placed on the  $ab$ -plane. Therefore, when the incident wave propagating along the  $z'$  direction transmits through the  $\perp$ -cut crystal (the crystal surface is the  $x'y'$ -plane) as shown in Fig. 4(b),  $A_u$  modes are not excited and only  $B_u$  modes are excited. In this case, the dielectric function is given by

$$\tilde{\epsilon}_{ij} = \epsilon_{ij}^{\infty} + \sum_{n \in \{B_u\}} \tilde{S}_n \Gamma_i(\phi_n) \Gamma_j(\phi_n) \quad (11)$$

for  $i, j \in \{x', y'\}$ , where  $\Gamma_{x'}(\phi_n) = \cos \phi_n$ ,  $\Gamma_{y'}(\phi_n) = \sin \phi_n$ , and  $\theta_n = \pi/2$  for  $B_u(x', y')$  modes. However, when the two dipole moments  $B_{u,1}$  and  $B_{u,2}$  are orthogonal with each other (*i.e.*,  $\phi_2 = \phi_1 + \pi/2$ ), the dielectric tensor elements in (11) becomes  $\phi_n$ -independent, because  $\tilde{\epsilon}_{x'x'} = \epsilon_{x'x'}^{\infty} + \tilde{S}_{B_{u,1}}$ ,  $\tilde{\epsilon}_{x'y'} = \epsilon_{x'y'}^{\infty}$ ,  $\tilde{\epsilon}_{y'y'} = \epsilon_{y'y'}^{\infty} + \tilde{S}_{B_{u,1}}$ , when  $\tilde{S}_{B_{u,1}} = \tilde{S}_{B_{u,2}}$  is assumed. Therefore, the isotropic behavior (no angle dependence) of the 0.96 THz mode excitation in the  $\perp$ -cut seraphinite

in Fig. 3(b) can be understood by the fact that there exist two  $B_u$  modes being orthogonal with each other and of the same resonant frequency at 0.96 THz.

### E. Anisotropic Excitation Behavior in the $\parallel$ -Cut Seraphinite

To understand the  $\parallel$ -cut measurement in Fig. 3(d), we assume that the sample was cut slightly tilted from the principal  $y'z'$  plane so that the dipole moments of the  $A_u$  modes are slightly tilted from the sample  $z'$ -axis. So, the  $(x', y', z')$  coordinates now represent the sample coordinate system, as depicted in Fig. 4(b). Then, the incident electric-field  $\mathbf{E}'_{x'y'z'}$  in the sample coordinates is represented through a coordinate transformation from the lab-frame measurements  $\mathbf{E}_{xyz}$  in Fig. 4(d), or

$$\mathbf{E}'_{x'y'z'} = [R_z(\phi)R_x(\theta)]\mathbf{E}_{xyz} \equiv M(\theta, \phi)\mathbf{E}_{xyz} \quad (12)$$

where each rotation operation  $R_j(\theta)$  represents the coordinate rotation by a counter-clockwise angle  $\theta$  about the  $j$ -axis.

The induced polarizability  $\tilde{P}'_{x'y'z'}$  in the sample coordinates is given, in terms of the linear electric susceptibility tensor  $\tilde{\chi}^{(1)}(\omega) = \tilde{\epsilon}(\omega) - \mathbf{I}$  and the electric-field  $\mathbf{E}'_{x'y'z'}$ , by

$$\tilde{P}'_{x'y'z'} = \epsilon_0 \begin{bmatrix} \tilde{\chi}_{x'x'}^{(1)} & \tilde{\chi}_{x'y'}^{(1)} & 0 \\ \tilde{\chi}_{x'y'}^{(1)} & \tilde{\chi}_{y'y'}^{(1)} & 0 \\ 0 & 0 & \tilde{\chi}_{z'z'}^{(1)} \end{bmatrix} \mathbf{E}'_{x'y'z'}. \quad (13)$$

The polarizability  $\tilde{P}_{xyz}$  in the lab-frame coordinates is then given by

$$\tilde{P}_{xyz} = M(\theta, \phi)^{-1} \tilde{P}'_{x'y'z'}. \quad (14)$$

When the incident electric wave is linearly-polarized along the  $z$ -axis, the angle dependence of the polarizability can be obtained from the  $z$ -component of  $\tilde{P}_{xyz}$  as a function of  $\theta$  as

$$\tilde{P}_z(\theta) = \epsilon_0 \tilde{\chi}_{x'x'}^{(1)} \sin^2 \theta + \epsilon_0 \tilde{\chi}_{z'z'}^{(1)} \cos^2 \theta \quad (15)$$

when  $\phi = 0$  is chosen in  $M$  for simplicity. Then, the  $\pi$  periodicity of the polarization angle for the  $B_u$  mode at 0.96 THz in Fig. 3(d) can be simply explained by the  $\theta$  dependence in (15).

However, the  $A_u$  modes at 0.8 THz and 1.2 THz have a period with  $\pi/2$ , which needs to be accounted for by higher-order polarizabilities. The monoclinic crystal in the space group of  $C2/m$  is centro-symmetric, so the next non-vanishing contribution is from the third-order susceptibility  $\tilde{\chi}^{(3)}$ , which is given in the sample coordinates  $(x', y', z')$  by

$$\tilde{\chi}_{ijkl}^{(3)}(\omega) = \sum_{n \in \{A_u, B_u\}} \tilde{S}_n(\omega) \Gamma_i^n \Gamma_j^n \Gamma_k^n \Gamma_l^n. \quad (16)$$

Then, the  $z$ -component of  $\tilde{P}_{xyz}^{(3)}$  is given by

$$\begin{aligned} \tilde{P}_z^{(3)} &= 3\epsilon_0 \sum_{ijkl} M_{zi}^{-1} \tilde{\chi}_{ijkl}^{(3)}(\omega) E_j(\omega) E_k(-\omega) E_l(\omega) \\ &= 3\epsilon_0 \sum_{n \in \{A_u, B_u\}} \tilde{S}_n [\sin^4 \theta_n \sin^4 \phi_n \sin^4 \theta + \cos^4 \theta_n \cos^4 \theta \\ &\quad + 6 \cos^2 \theta_n \sin^2 \theta_n \sin^2 \phi_n \cos^2 \theta \sin^2 \theta]. \end{aligned} \quad (17)$$

Fig. 5 shows the measured  $\text{Im}[\tilde{\chi}_{\text{eff}}]$  numerically fitted, respectively, to (15) for 0.96 THz and to (17) for 0.80 and 1.20 THz. The tilting angles of the  $A_u$  modes, with respect to the  $z'$ -axis,

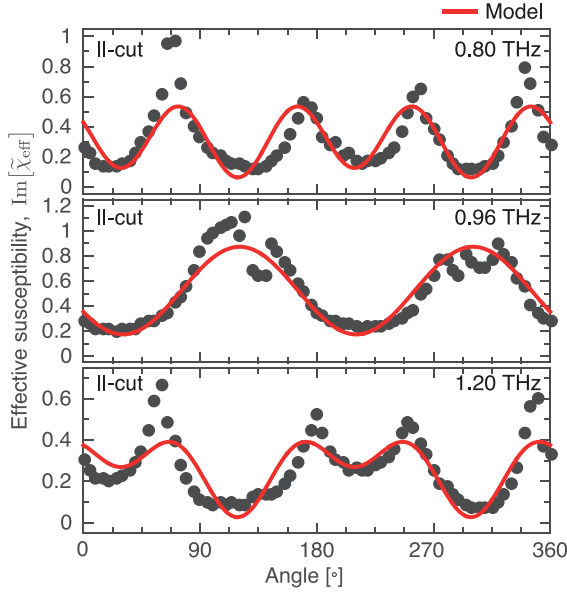


Fig. 5. Effective susceptibility  $\chi_{\text{eff}}$  of the ||-cut seraphinite is extracted by (10).  $\chi_{\text{eff}}$  (0.96 THz) for  $B_u$  is fitted to (15). And  $\chi_{\text{eff}}$  (0.8 THz) and  $\chi_{\text{eff}}$  (1.20 THz) corresponding to  $A_u$  modes are fitted to (17) represented by the red solid line.

are obtained as  $\theta_1 = 228^\circ$ ,  $\phi_1 = -120^\circ$  for 0.8 THz and  $\theta_2 = -139^\circ$ ,  $\phi_2 = -117^\circ$  for 1.20 THz.

#### IV. DISCUSSION

We now turn our attention to the origin of the observed THz absorptions. First of all, the possibility of water vapor absorption [40], which occurs at 26 and 58  $\text{cm}^{-1}$ , is excluded by the subsequent temperature dependence of the mode frequency at elevated temperatures. To our knowledge, scientific literatures regarding seraphinite, or even including most hydrous/anhydrous layered silicates, are very limited and theoretical prediction is not available for phonon modes. Therefore, we can compare with indirect information regarding chlorite, which has similar local bonding networks of Si-O and Mg-O in their block-layered structures. In a chlorite mineral, far infrared absorptions are observed [41] at 120, 140, and 220  $\text{cm}^{-1}$ . In addition, inelastic neutron scattering (INS) of chlorite reveals that there is only acoustic phonon branch below 1.5 THz [42], which can be Raman-active at  $\sim 50 \text{ cm}^{-1}$ . The phonon modes of chlorite can be inferred from the theoretical and experimental results on a magnesium-olivine, forsterite ( $\text{Mg}_2\text{SiO}_4$ ). Forsterite is composed of isolated silicate tetrahedra but shares the same local bonding of Si-O and Mg-O with a chlorite. The zone boundary acoustic mode is calculated at 100  $\text{cm}^{-1}$  [43] and the optic modes are calculated at 130, 180, and 250  $\text{cm}^{-1}$  [44]. In our speculation, the obtained near 1-THz resonances in seraphinite originate from the unique structure that has electrically charged layers (talc-like layer and brucite-like layer) [28], although we cannot directly prove it without DFT calculation. In that regards, not all sheet silicate minerals necessarily have resonances in THz frequency region. Therefore, we explain the absorption peak at 0.96 THz of seraphinite phenomenologically in the context of the phonon-polariton coupled mode. It can be understood that the infrared (IR)-active phonon modes are originated

from its monoclinic crystalline structure with the space group of C2/m [30]–[32].

The dispersion relation can be obtained by considering the relative dielectric function  $\tilde{\epsilon}$  which is defined for an applied electric-field  $\tilde{E}$  and the induced polarizability  $\tilde{P}$  as [45]

$$\tilde{\epsilon}(\omega) = \frac{\epsilon(\omega)}{\epsilon_0} = 1 + \frac{1}{\epsilon_0} \frac{\tilde{P}(\omega)}{\tilde{E}(\omega)}. \quad (18)$$

When the dielectric function  $\tilde{\epsilon}$  of (18) is written in terms of the longitudinal and transverse modes (LO and TO), (18) is reduced to a factorized form of its poles and zeros given by [46]

$$\tilde{\epsilon}(\omega) = \epsilon^\infty \prod_{j=1}^N \frac{\Omega_{\text{LO}j}^2 - \omega^2 - i\omega\Gamma_{\text{LO}j}}{\Omega_{\text{TO}j}^2 - \omega^2 - i\omega\Gamma_{\text{TO}j}} \quad (19)$$

where  $\epsilon^\infty$  is the high frequency dielectric constant,  $\Omega_{\text{TO}j}$  ( $\Omega_{\text{LO}j}$ ) and  $\Gamma_{\text{TO}j}$  ( $\Gamma_{\text{LO}j}$ ) are the resonant frequency and the damping constant of the  $j$ th TO (LO) mode, respectively. By substituting zero for angular frequency  $\omega$  of (19) [47], the zero frequency dielectric constant is obtained as

$$\tilde{\epsilon}(0) = \epsilon^\infty \prod_{j=1}^N \frac{\Omega_{\text{LO}j}^2}{\Omega_{\text{TO}j}^2} \quad (20)$$

which is the Lyddane–Sachs–Teller (LST) relation [48]. When we assume zero damping in (19), the Kurosawa formula [49] is obtained as

$$\tilde{\epsilon}(\omega) = \epsilon^\infty \prod_{j=1}^N \frac{\Omega_{\text{LO}j}^2 - \omega^2}{\Omega_{\text{TO}j}^2 - \omega^2}. \quad (21)$$

So, the phonon-polariton dispersion is obtained using either (19) or (21), which is given by

$$\frac{c^2 \tilde{k}^2(\omega)}{\omega^2} = \tilde{n}^2(\omega) = \tilde{\epsilon}(\omega) \quad (22)$$

where  $\tilde{n}$  is the complex index of refraction defined in (2) and  $\tilde{k}(\omega)$  is the complex wave vector.

However, since the measured range of frequency is limited to 2 THz, (22) needs correction [29]. When we apply the parameter  $\epsilon_{\text{exp}}$  defined by

$$\epsilon_{\text{exp}} = \epsilon^\infty \prod_{j=2}^N \frac{\Omega_{\text{LO}j}^2}{\Omega_{\text{TO}j}^2} \quad (23)$$

to the measured data, the modified phonon-polariton dispersion for a single mode is given by

$$\tilde{k}(\omega) = \frac{\omega}{c} \left[ \epsilon_{\text{exp}} \frac{\Omega_{\text{LO}1}^2 - \omega^2 - i\omega\Gamma_{\text{LO}1}}{\Omega_{\text{TO}1}^2 - \omega^2 - i\omega\Gamma_{\text{TO}1}} \right]^{1/2}. \quad (24)$$

It is noted that the fitting parameter  $\epsilon_{\text{exp}}$  is a experimentally measured dielectric constant at the highest frequency throughout the measured frequency range from 0.2 to 2 THz.

Fig. 6 shows the phonon-polariton dispersion curve [ $\omega$  vs.  $k(\omega)$ ] (closed circles) retrieved from the measurement of the  $\perp$ -cut sample at  $\theta = 120^\circ$ . The real part of  $\tilde{k}(\omega)$  is

$$\text{Re}[\tilde{k}(\omega)] = \frac{\omega}{c} \sqrt{\tilde{n}^2(\omega) + \kappa^2(\omega)} \quad (25)$$

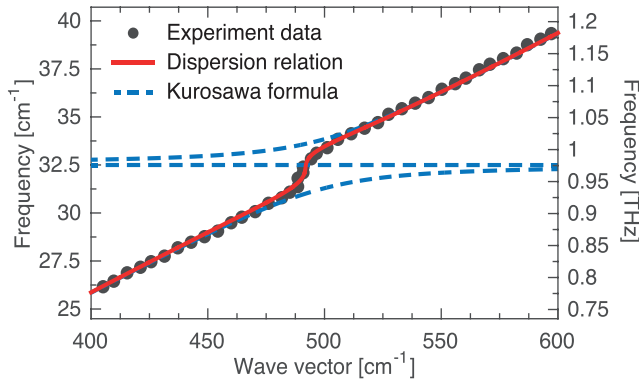


Fig. 6. Phonon-polariton dispersion of the experimental results of  $\perp$ -cut seraphinite measured at azimuthal angle of  $120^\circ$ . The dispersion relation and the experimental data are indicated with red solid line and closed circles, respectively. The dispersion relation and the measured data are plotted with the real part of (24) and (25), respectively. The Kurosawa formula is represented with blue dotted line, which is also computed using the real part of (24) in the case of no damping.

which is shown in comparison with the theoretical guide (red solid line) calculated from the real part of (24). The Kurosawa formula (blue dotted line) is also computed using the real part of (24) in the case of no damping. It is noted that  $(\varepsilon_{\text{exp}})^{1/2}$  can be extracted by  $\sqrt{n^2(\omega) + \kappa^2(\omega)}|_{\omega \rightarrow \omega^\infty}$  in (25), where  $\omega^\infty$  represents the highest frequency component. The fitting parameters in the unit of  $\text{cm}^{-1}$  are estimated from the measurement as  $\Omega_{\text{TO}_1} = 32.5 \text{ cm}^{-1}$ ,  $\Omega_{\text{LO}_1} = 32.6 \text{ cm}^{-1}$ ,  $\Gamma_{\text{TO}_1} = 2.74 \text{ cm}^{-1}$ ,  $\Gamma_{\text{LO}_1} = 2.67 \text{ cm}^{-1}$ , and  $(\varepsilon_{\text{exp}})^{1/2} = 2.44$  for the  $\perp$ -cut seraphinite. The splitting ( $0.1 \text{ cm}^{-1} = 3 \text{ GHz}$ ) is about three times smaller than the spectral resolution ( $10 \text{ GHz} = 1/T$  and  $T = 100 \text{ ps}$ ) in our THz-TDS. So, the  $\Omega_{\text{TO}_1}$  and  $\Omega_{\text{LO}_1}$  extracted through numerical fitting for the resonance at 0.96 THz should be understood as  $\Omega_{\text{TO}_1} = 32.5 \pm 0.17 \text{ cm}^{-1}$ ,  $\Omega_{\text{LO}_1} = 32.6 \pm 0.17 \text{ cm}^{-1}$ . It is noted that  $\Omega_{\text{LO}_1}$  is bigger than  $\Omega_{\text{TO}_1}$  ( $\Omega_{\text{LO}_j} > \Omega_{\text{TO}_j}$ ) since  $\varepsilon^\infty$  is in general smaller than  $\varepsilon(0)$  by the LST relation for all the optical phonon modes [48]–[50]. Provided  $1/\omega$  is substituted by  $\xi$ , the factorized dielectric function of (19) can be expanded for  $\xi \rightarrow 0$  in the form [46]

$$\tilde{\varepsilon}(\omega) \simeq \varepsilon^\infty \prod_{j=1}^N [1 + i\Gamma_{\text{LO}_j}\xi + O(\xi^2)] \times [1 - i\Gamma_{\text{TO}_j}\xi + O(\xi^2)]|_{\xi \rightarrow 0}. \quad (26)$$

By further calculation, (26) is equivalent to

$$\tilde{\varepsilon}(\omega) \simeq \varepsilon^\infty \left[ 1 + i \sum_{j=1}^N (\Gamma_{\text{LO}_j} - \Gamma_{\text{TO}_j})\xi \right]|_{\xi \rightarrow 0} \quad (27)$$

which is the generalized form of Lowndes condition for all IR-active branches induced by Schubert [46], [51]. Equation (27) for  $\text{Im}[\tilde{\varepsilon}(\omega)] > 0$  shows that there are the optical phonons with conditions for  $\Gamma_{\text{LO}} < \Gamma_{\text{TO}}$  as well as  $\Gamma_{\text{LO}} > \Gamma_{\text{TO}}$  satisfying  $\sum_{j=1}^N (\Gamma_{\text{LO}_j} - \Gamma_{\text{TO}_j})\xi > 0$  [46]. The resonance mode at 0.96 THz of  $\perp$ -cut is expected as one of the optical modes with  $\Gamma_{\text{LO}} < \Gamma_{\text{TO}}$ . Therefore, the above theoretical interpretation based on Kurosawa formula with and without the damping terms shows an excellent agreement with the observed dispersion anisotropy in the THz frequency range.

## V. CONCLUSION

In summary, we have reported a spectral fingerprint of crystal seraphinite, a type of gemstone, in THz frequency range. In our measurements conducted with THz-TDS, the strong IR-active modes at 0.80, 0.96, and 1.20 THz in seraphinite have been found. In particular, the 0.96 THz mode has exhibited a strong and narrow ( $Q = 8$ ) absorption, comparable to the previously reported 0.53 THz mode in  $\alpha$ -lactose monohydrate. The polarization-dependent THz-TDS measurements have furthermore revealed the birefringence of the investigated crystal originated from its crystalline monoclinic structure with the space group  $C2/m$  and also the  $A_u(z')$ -symmetry of the 0.80 and 1.20 THz modes and the  $B_u(x', y')$ -symmetry of the 0.96 THz mode. Theoretical interpretation based on the Kurosawa formula has shown an excellent agreement with the observed phonon-polariton dispersion anisotropy.

THz absorption lines in solid-state materials are rare and, in particular, there have been no known spectral lines for gemstones in THz frequency range. Gems are often optically superior materials and thus optical gemology that utilizes visible, near-infrared, UV, and even X-rays light sources, has been established to study and characterize gems. However, to the best of our knowledge, THz waves have never been used so far for that purpose. It is hoped that THz spectroscopy may become useful for identification and characterization of various gemstones.

## ACKNOWLEDGMENT

The authors thank C.-S. Woo, Dr. A. T. Lee, Prof. C. H. Yang, Prof. M. J. Han, and Prof. Y. H. Kim for fruitful discussions.

## REFERENCES

- [1] M. Tonouchi, "Cutting-edge terahertz technology," *Nat. Photon.*, vol. 1, p. 97, 2007.
- [2] Y.-S. Lee, *Principles of Terahertz Science and Technology*, 1st ed. New York, NY, USA: Springer, 2008.
- [3] D. Grischkowsky, S. Keiding, M. Vanexter, and C. Fattinger, "Far-infrared time-domain spectroscopy with terahertz beams of dielectrics and semiconductors," *J. Opt. Soc. Am. B*, vol. 7, p. 2006, 1990.
- [4] B. Ferguson and X. C. Zhang, "Materials for terahertz science and technology," *Nat. Mater.*, vol. 1, p. 26, 2002.
- [5] Y. H. K. G.-S. Park, H. Han, J. K. Han, J. Ahn, J.-H. Son, W.-Y. Park, and Y. U. Jeong, *Convergence of Terahertz Sciences in Biomedical Systems*. New York, NY, USA: Springer, 2012.
- [6] P. C. M. Planken, H. K. Nienhuys, H. J. Bakker, and T. Wenckebach, "Measurement and calculation of the orientation dependence of terahertz pulse detection in ZnTe," *J. Opt. Soc. Am. B*, vol. 18, p. 313, 2001.
- [7] W. Withayachumnankul, B. Ferguson, T. Rainsford, S. P. Mican, and D. Abbott, "Simple material parameter estimation via terahertz time-domain spectroscopy," *Electron. Lett.*, vol. 41, p. 800, 2005.
- [8] Y. S. Jin, G. J. Kim, and S. G. Jeon, "Terahertz dielectric properties of polymers," *J. Kor. Phys. Soc.*, vol. 49, p. 513, 2006.
- [9] J. Chen, Y. Q. Chen, H. W. Zhao, G. J. Bastiaans, and X. C. Zhang, "Absorption coefficients of selected explosives and related compounds in the range of 0.1–2.8 THz," *Opt. Express*, vol. 15, p. 12060, 2007.
- [10] D. S. Venables and C. A. Schmuttenmaer, "Far-infrared spectra and associated dynamics in acetonitrile-water mixtures measured with femtosecond THz pulse spectroscopy," *J. Chem. Phys.*, vol. 108, p. 4935, 1998.
- [11] J. H. Son, "Terahertz electromagnetic interactions with biological matter and their applications," *J. Appl. Phys.*, vol. 105, p. 102033, 2009.
- [12] H. T. Chen, W. J. Padilla, J. M. O. Zide, A. C. Gossard, A. J. Taylor, and R. D. Averitt, "Active terahertz metamaterial devices," *Nature*, vol. 444, p. 597, 2006.

- [13] M. Naftaly and R. E. Miles, "Terahertz time-domain spectroscopy of silicate glasses and the relationship to material properties," *J. Appl. Phys.*, vol. 102, p. 043517, 2007.
- [14] D. Han, K. Lee, J. Lim, S. S. Hong, Y. K. Kim, and J. Ahn, "Terahertz lens made out of natural stone," *Appl. Optics*, vol. 52, p. 8670, 2013.
- [15] M. Janek, I. Bugár, D. Lorenc, V. Szöcs, D. Velič, and D. Chorvát, "Terahertz time-domain spectroscopy of selected layered silicates," *Clays and Clay Miner.*, vol. 57, p. 416, 2009.
- [16] Y. Kim, J. Ahn, B. G. Kim, and D. S. Yee, "Terahertz birefringence in zinc oxide," *Jpn. J. Appl. Phys.*, vol. 50, p. 030203, 2011.
- [17] G. Acbas, K. A. Niessen, E. H. Snell, and A. G. Markelz, "Optical measurements of long-range protein vibrations," *Nat. Commun.*, vol. 5, p. 3076, 2014.
- [18] J. Kröll, J. Darmo, and K. Unterrainer, "Terahertz optical activity of sucrose single-crystals," *Vib. Spectrosc.*, vol. 43, p. 324, 2007.
- [19] O. Ostroverkhova, D. Cooke, F. Hegmann, R. Tykwinski, S. Parkin, and J. Anthony, "Anisotropy of transient photoconductivity in functionalized pentacene single crystals," *Appl. Phys. Lett.*, vol. 89, p. 192113, 2006.
- [20] D. J. Aschaffenburg, M. R. C. Williams, D. Talbayev, D. F. Santavica, D. E. Prober, and C. A. Schmuttenmaer, "Efficient measurement of broadband terahertz optical activity," *Appl. Phys. Lett.*, vol. 100, p. 241114, 2012.
- [21] A. M. Shuvaev, G. V. Astakhov, A. Pimenov, C. Brune, H. Buhmann, and L. W. Molenkamp, "Giant magneto-optical Faraday effect in HgTe thin films in the terahertz spectral range," *Phys. Rev. Lett.*, vol. 106, p. 107404, 2011.
- [22] H. Kim, M. Yi, X. Y. Wang, S. W. Cheong, and J. Ahn, "Ultrafast terahertz transmission ellipsometry of  $\text{YMn}_2\text{O}_5$  electromagnons," *Appl. Phys. Lett.*, vol. 101, p. 242911, 2012.
- [23] G. Xuejiao, X. Wei, and S. Jingling, "THz spectroscopy and polarization of jade," in *Proceedings of SPIE*, 2010, vol. 7854, p. 78542H.
- [24] J. W. Anthony, *Handbook of Mineralogy*. Tucson, Ariz.: Mineral Data Pub., 1990.
- [25] M. D. Welch and W. G. Marshall, "High-pressure behavior of clinocllore," *Am. Mineral.*, vol. 86, p. 1380, 2001.
- [26] A. C. Rule and S. W. Bailey, "Refinement of the crystal-structure of a monoclinic ferroan clinocllore," *Clays and Clay Miner.*, vol. 35, p. 129, 1987.
- [27] C. K. Kohut and C. J. Warren, J. B. Dizon and D. G. Schulze, Eds., "Chlorites," in *Soil Mineralogy With Environmental Applications*. USA: Soil Science Society of America, 2002, edited by.
- [28] G. E. Spinnler, P. G. Self, S. Iijima, and P. R. Buseck, "Stacking disorder in clinocllore chlorite," *Am. Mineral.*, vol. 69, p. 252, 1984.
- [29] S. Kojima, N. Tsumura, M. W. Takeda, and S. Nishizawa, "Far-infrared phonon-polariton dispersion probed by terahertz time-domain spectroscopy," *Phys. Rev. B*, vol. 67, p. 035102, 2003.
- [30] N. B. Colthup, L. H. Daly, and S. E. Wiberley, *Introduction to Infrared and Raman Spectroscopy*, 3rd ed. Boston, MA, USA: Academic, 1990.
- [31] F. A. Cotton, *Chemical Applications of Group Theory*, 3rd ed. New York, NY, USA: Wiley, 1990.
- [32] W. G. Fateley, *Infrared and Raman Selection Rules for Molecular and Lattice Vibrations: The Correlation Method*. New York: Wiley-Interscience, 1972.
- [33] R. W. Boyd, *Nonlinear Optics*, 3rd ed. Amsterdam, Boston: Academic Press, 2008.
- [34] E. R. Brown, J. E. Bjarnason, A. M. Fedor, and T. M. Korter, "On the strong and narrow absorption signature in lactose at 0.53 THz," *Appl. Phys. Lett.*, vol. 90, p. 061908, 2007.
- [35] A. M. Hofmeister, E. Keppel, and A. K. Speck, "Absorption and reflection infrared spectra of MgO and other diatomic compounds," *Mon. Not. R. Astron. Soc.*, vol. 345, p. 16, 2003.
- [36] A. B. Kuzmenko, E. A. Tishchenko, and V. G. Orlov, "Transverse optic modes in monoclinic  $\alpha\text{-Bi}_2\text{O}_3$ ," *J. Phys.: Condens. Mat.*, vol. 8, p. 6199, 1996.
- [37] T. Moller, P. Becker, L. Bohaty, J. Hemberger, and M. Gruninger, "Infrared-active phonon modes in monoclinic multiferroic  $\text{MnWO}_4$ ," *Phys. Rev. B*, vol. 90, p. 155105, 2014.
- [38] J. R. Aronson, A. G. Emslie, E. V. Miseso, E. M. Smith, and P. F. Strong, "Optical-constants of monoclinic anisotropic crystals—Gypsum," *Appl. Opt.*, vol. 22, p. 4093, 1983.
- [39] J. D. Jackson, *Classical Electrodynamics*, 3rd ed. New York, NY, USA: Wiley, 1999.
- [40] S. A. Fitzgerald and A. J. Sievers, "Lattice phonon modes in solid C-60 studied by far-infrared spectroscopy—Comment," *Phys. Rev. Lett.*, vol. 70, p. 3175, 1993.
- [41] C. Koike, H. Hasegawa, and T. Hattori, "Mid-infrared and far-infrared extinction coefficients of hydrous silicate minerals," *Astrophys. Space Sci.*, vol. 88, p. 89, 1982.
- [42] D. R. Collins, W. G. Stirling, C. R. A. Catlow, and G. Rowbotham, "Determination of acoustic phonon-dispersion curves in layer silicates by inelastic neutron-scattering and computer-simulation techniques," *Phys. Chem. Miner.*, vol. 19, p. 520, 1993.
- [43] K. R. Rao, S. L. Chaplot, N. Choudhury, S. Ghose, and D. L. Price, "Phonon density of states and specific-heat of forsterite,  $\text{Mg}_2\text{SiO}_4$ ," *Science*, vol. 236, p. 64, 1987.
- [44] K. R. Rao *et al.*, "Lattice-dynamics and inelastic neutron-scattering from forsterite,  $\text{Mg}_2\text{SiO}_4$ : Phonon-dispersion relation, density of states and specific-heat," *Phys. Chem. Miner.*, vol. 16, p. 83, 1988.
- [45] F. Gervais and B. Piriou, "Temperature-dependence of transverse-optic and longitudinal-optic modes in  $\text{TiO}_2$  (rutile)," *Phys. Rev. B*, vol. 10, p. 1642, 1974.
- [46] M. Schubert, T. Tiwald, and C. Herzinger, "Infrared dielectric anisotropy and phonon modes of sapphire," *Phys. Rev. B*, vol. 61, p. 8187, 2000.
- [47] D. W. Berreman and F. C. Unterwald, "Adjusting poles and zeros of dielectric dispersion to fit reststrahlen of  $\text{PrCl}_3$ , and  $\text{LaCl}_3$ ," *Phys. Rev.*, vol. 174, p. 791, 1968.
- [48] A. S. Barker, "Transverse and longitudinal optic mode study in  $\text{MgF}_2$ , and  $\text{ZnF}_2$ ," *Phys. Rev.*, vol. 136, p. A1290, 1964.
- [49] T. Kurosawa, "Polarization waves in solids," *J. Phys. Soc. Jpn.*, vol. 16, no. 7, p. 1298, 1961.
- [50] C. Kittel, *Introduction to Solid State Physics*. Hoboken, NJ, USA: Wiley, 2005.
- [51] R. P. Lowndes, "Influence of lattice and harmonicity on the longitudinal optic modes of cubic ionic solids," *Phys. Rev. B*, vol. 1, p. 2754, 1970.

**Dae-hoon Han**, photograph and biography not available at time of publication.

**Heejae Jeong**, photograph and biography not available at time of publication.

**Yunheung Song**, photograph and biography not available at time of publication.

**Jai Seok Ahn**, photograph and biography not available at time of publication.

**Jaewook Ahn**, photograph and biography not available at time of publication.